Structural Durability & Health Monitoring

Tech Science Press

https://doi.org/10.32604/sdhm.2026.081510

ARTICLE

Investigation of the Mechanism of Temperature-Induced Fatigue at the Epoxy-Emulsified Asphalt Micro-Surfacing Interface Using DIC and Fracture Mechanics

Dongjie Tan[1], **Xiaoyu Yang**[2] **and Xinxin Cao**[3,*]

[1]Shanghai Municipal Engineering Design Institute (Group) Co., Ltd., Shanghai, China
[2]School of Traffic and Transportation, Chongqing Jiaotong University, Chongqing, China
[3]Department of Road and Urban Railway Engineering, Beijing University of Technology, Beijing, China

*Corresponding Author: Xinxin Cao. Email: caoxinxin@sdut.edu.cn

Received: 03 March 2026; Accepted: 29 April 2026; Published: 24 August 2026

ABSTRACT: Interfacial adhesion failure is the primary limiting factor in the long-term durability of epoxy-emulsified asphalt micro-surfacing pavements. However, while digital image correlation (DIC) has been extensively applied to evaluate the bulk fatigue of traditional hot-mix asphalt and concrete, its specific application to the complex bi-material interface between rigid concrete substrates and cold-mixed, thermosetting epoxy-asphalt overlays remains limited. Consequently, current research lacks real-time data on full-field strain evolution and the transitional damage localisation mechanisms during dynamic fatigue processes under extreme temperature gradients. To this goal, three-point bending fatigue tests were performed at various temperatures (ranging from −10°C to 45°C). The fatigue damage behaviour at the contact was quantified by combining digital image correlation (DIC) with fracture mechanics calculations. The results show that the fatigue life at the contact follows a non-monotonic "bell-shaped" trend, peaking at 15°C. At a low temperature of −10°C, fatigue life is reduced by 78% compared to the peak value. DIC research indicated that strain localisation was the dominant failure mode, resulting in brittle fracture. At 45°C, despite an exponential increase in the interfacial fracture energy release rate (G_c) due to viscous dissipation, fatigue life was reduced by 90%. At 45°C, the interfacial failure mechanism transitions from localised crack propagation to extensive viscoplastic shear flow. This indicates that high-temperature failure is primarily driven by matrix softening and a critical loss of internal shear strength. The findings suggest that the enhancement in performance at 15°C is attributable to the synergistic interaction between the epoxy resin network (which provides stiffness) and the bituminous phase (which promotes relaxation). This method has been demonstrated to be an effective means of preventing both low-temperature brittleness and high-temperature viscoelastic deformation.

KEYWORDS: Epoxy-emulsified asphalt micro-surfacing; interface fatigue; three-point bending fatigue; digital image correlation technology; temperature effects

1 Introduction

Micro-surfacing technology is a low-cost preventative maintenance method that is widely utilised around the world to restore pavement surface performance and extend its service life [1–3]. However, as a typical thin overlay structure, the bond strength at the interface between micro-surfacing and the existing pavement, particularly hard cement concrete pavements, is important to its long-term durability [4,5]. In actual service, the contact is subjected to recurrent shear stress from vehicle loads as well as difficulties from dramatic external temperature variations. Existing engineering practices show that interlayer delamination has emerged as the dominant failure mode causing premature deterioration of micro-surfacing (e.g., delamination and spalling) [2,6]. The interface, particularly in "rigid base course + thin overlay" systems, must not only transmit traffic shear forces but also withstand complicated stress concentrations generated by thermal contraction or base course cracking [7].

Existing evaluation techniques include the Layer-to-Layer Shear Test (LPDS) developed by Raab and Partl [8] and the pull-off test promoted by West [9]. These methods have become widely used for determining interfacial bond strength. However, the aforementioned static tests largely characterise the interface's ultimate potential to resist pure shear or pure tensile failure in a single direction, failing to adequately mimic the most severe failure mechanism in composite pavement structures: reflected cracks [10,11]. According to Zhou and Scullion [12], Reflecting cracking consists primarily of cracks that originate at the base layer joints and propagate upward through the interface layer due to the combined impacts of traffic loads and temperature cycles. Instead of simple horizontal shear, the interface region suffers highly concentrated coupled bending tension and shear forces. Recent numerical simulations [13] have also revealed that monotonic shear strength measurements overestimate interfacial fatigue life while failing to predict crack-tip-driven debonding behaviour. As a result, the three-point bending fatigue test (3PB) subjected the interface region to high flexural stress conditions, effectively replicating the crack propagation process from the base layer up through the interface [14–16]. Saride and Kumar [17] used this apparatus to assess the crack-resistant performance of geosynthetic interlayers, demonstrating that the bending mode better represents the actual conditions of structural interlayer failure. In addressing issues such as fatigue cracking, Albayati et al. [18] employed a method of modifying bituminous binders using nanomaterials and polymers, and evaluated the effects of NS, NHL, SBS and EVA on the performance of the bituminous binder. The findings demonstrated that the SBS-modified binder demonstrated superior resistance to rutting and fatigue; modification with nanomaterials also enhanced the binder's stiffness and high-temperature stability. In their review, Zhou et al. [19] demonstrated that the introduction of nano- or micron-scale fillers into polymer matrices—such as ceramic fillers (e.g., silica nanoparticles), carbonaceous fillers (e.g., carbon nanotubes) and clay fillers—can effectively improve the matrix's mechanical properties, interfacial bond strength and environmental adaptability, thereby extending the material's fatigue life. However, while these physical modifications improve conventional asphalt, the introduction of a thermosetting epoxy resin network into emulsified asphalt (epoxy-emulsified asphalt, EEA) creates a fundamentally different, cross-linked internal structure. Unlike hot-mix epoxy asphalt, which is well-documented for steel bridge deck pavements, cold-mixed EEA micro-surfacing presents unique temperature-dependent rheological behaviours. The micro-mechanical interaction of this specific cross-linked network with a rigid cement concrete base course under dynamic thermal-mechanical coupling remains poorly understood.

In the study of fatigue damage mechanisms, traditional linear variable differential transformers (LVDTs) or strain gauges can only capture the macroscopic deformation of specimens or single-point strain. Bhasin and Little [20] observed that asphalt-based composites are highly heterogeneous, and typical macroscopic measurements only record the average strain within the gauge length. Digital image correlation (DIC) is a non-contact, full-field optical measurement technology that produces high-precision full-field strain maps [21]. Sudarsanan et al. [22] and Ren et al. [23] used DIC to demonstrate the presence of considerable strain localisation in asphalt mixtures. Strain tends to concentrate preferentially at the interface between aggregates and binder, resulting in narrow zones of high gradient. These locations act as nucleation sites for macroscopic cracks. Seo et al. [24] used DIC to quantify the size of the fracture propagation zone (FPZ), demonstrating that a diffusion-type damage zone had formed within the material before the appearance of macroscopic cracks. Huang et al. [25] successfully applied DIC to investigate brittle fracture in concrete. However, there is a lack of systematic visual and quantitative research on the strain evolution patterns at the interface of epoxy-emulsified asphalt micro-surfacing during temperature cycling. Despite these advancements, existing DIC research predominantly focuses on the homogeneous bulk failure of individual materials (e.g., pure concrete or single asphalt mixtures). Capturing the fatigue degradation at a bi-material interface, specifically between a purely rigid substrate and a highly temperature-sensitive, viscoelastic-thermosetting EEA matrix, presents unique experimental challenges. There is a notable lack of systematic, visual, and quantitative research tracking the continuous transition of failure modes (from brittle fracture to viscoplastic shear flow) at the micro-surfacing interface across a wide temperature spectrum.

To fill the aforementioned research gap and distinguish the unique interfacial behaviour of the EEA system from traditional asphalt composites, this study seeks to uncover the nonlinear regulation mechanism of temperature on fatigue failure at the interface of cement concrete and epoxy-emulsified asphalt micro-surfacing. This work uses stress-controlled three-point bending fatigue tests to model the interfacial stress condition caused by reflected cracks. When combined with high-resolution DIC technology, it allows for real-time monitoring of full-field strain evolution over a large temperature range of −10°C to 45°C. This work attempts to establish the intrinsic relationship between temperature, micro-strain processes, and macro-fatigue life by combining fatigue life analysis, interfacial fracture energy release rate (G_c) computation, and failure morphology observations. This establishes a theoretical foundation for tackling spalling concerns induced by reflecting fissures in micro-surfacing.

2 Experimental Section

2.1 Experimental Materials

The test used C40 cement concrete as the base course simulation material, with a mix design that included cement, river sand, crushed stone, water, and a water-reducing agent. The surface treatment combination mix design contained high-performance epoxy emulsified asphalt, aggregate gradation that met ISSA Type III standards (Table 1), cement, water, and a lignin fibre additive. The base binder employed for emulsification is pure bitumen, with a penetration grade of 70#. The thermosetting modifier is constituted of a water-based bisphenol A (E-51) epoxy resin, which is characterised by excellent chemical stability and compatibility with bitumen emulsions. In order to initiate the cross-linking reaction at room temperature, it is necessary to select a suitable water-based polyamide or modified aliphatic amine as the curing agent. To quantitatively characterise the fundamental physical and mechanical properties of the prepared EEA binder, fundamental performance tests were conducted. The results of these tests are summarised in Table 2, which also presents the measured technical specifications.

Table 1: Aggregate gradation.

Sieve Size (mm)	**9.5**	**4.75**	**2.36**	**1.18**	**0.6**	**0.3**	**0.15**	**0.075**
Per cent passing (%)	100	95.2	68.5	45.3	30.1	19.8	13.5	8.2
ISS Specification Range	100	90–100	65–90	45–70	30–50	19–34	12–25	7–15

Table 2: Key technical specifications of epoxy resin adhesives.

Test Items	Unit	Technical Requirements	Typical Results	Test Methods
Solid content (25°C)	%	≥25	30	GB/T 11175
Surface drying time (25°C)	h	≤6	4	GB/T 1728
Touch-dry time (25°C)	h	≤24	12	GB/T 1728
Heat resistance (60°C)	–	No movement/sliding	through	GB/T 328.11
Tensile strength (25°C)	MPa	≥0.20	0.3	GB/T 2567
Bond strength with concrete (25°C)	MPa	≥0.20	0.3	ASTM D4541

2.2 Experimental Design

(1) Preparation of Cement Concrete

Table 3 shows the simulated base layer material for the test, which was C40 cement concrete. A measured amount of cement, river sand, and crushed stone was combined on a metal plate and thoroughly mixed. A suitable amount of water and a water-reducing agent were then added and stirred evenly. After complete mixing, the material was uniformly poured into a 10 cm × 10 cm × 10 cm mould for formation. It was compressed with an iron rod and covered once formed. The mould was removed after lying at room temperature for 24–48 h. The specimen was placed in a normal curing chamber (temperature 20 ± 2°C, humidity ≥95%) and tested after 28 days. To ensure a standardised and high-quality interfacial bond, the top surfaces of the 28-day cured C40 concrete base specimens were mechanically brushed to remove laitance and expose fine aggregates, followed by cleaning with high-pressure air and deionised water. The surface roughness was quantified using the Sand Patch Method (ASTM E965), yielding a consistent Mean Texture Depth (MTD) of 0.50 ± 0.08 mm across all specimens.

Table 3: Mass of components in cement concrete.

Materials	Quality (g)	Mass Ratio
Cement	362	
River sand	731	
Crushed stone	1097	1:0.580:2.019:3.031:0.005
Water	210	
Water-reducing agent	1.81	

(2) Preparation of Asphalt Micro-surfacing

Prepare the micro-surfacing mixture using the component weights listed in Table 4. At room temperature, thoroughly mix the weighed aggregates, filler, and cement. Add the appropriate amount of water and stir for 30 s. Mix in the adjusted emulsified asphalt and time it until it loses fluidity and sets (≥120 s).

(3) Preparation of Composite Specimens

After drying, the surface of the cement concrete base course must be properly cleaned with a brush to ensure that it is free of pollution. The foundation course will be set in a 10 cm × 10 cm × 20 cm mould. After applying a 5 mm thick layer of asphalt micro-surfacing, place another cured 10 cm × 10 cm × 10 cm cement test cube into the mould. The assembly will be kept undisturbed for 4 h. The 10 cm × 10 cm × 20 cm composite specimen was crushed using a rammer and cured at room temperature

(25 ± 2°C, RH 60 ± 5%) for 7 days. Micro-surfacing is applied directly onto the concrete base without any bonding layer. This approach evaluates the intrinsic chemical affinity and self-adhesive properties of the epoxy-emulsified asphalt binder while preventing third-party intermediate layers from interfering with the interfacial strain evolution monitored by DIC.

Table 4: Mass of components in asphalt micro-surfacing.

Materials	Quality (g)	Mass Ratio
Aggregate	88.5	100:11.8:8.2:1.2:0.3
Epoxy emulsified bitumen	10.44	
Water	7.26	
Cement	1.06	
Additives	0.265	

2.3 Cyclic Load Fatigue Testing

Composite specimens were tested using a dynamic universal testing equipment with a climate chamber (temperature control range: −20°C to 60°C). Before testing, specimens were placed in a climate chamber at various temperatures and conditioned for 4 h. Stress-controlled cyclic loading was performed at temperatures of −10°C, 0°C, 15°C, 30°C, and 45°C using a 10 Hz half-sine wave loading waveform. Stress-controlled cyclic loading was performed at temperatures of −10°C, 0°C, 15°C, 30°C, and 45°C, utilising a 10 Hz half-sine wave loading waveform.

In order to address the temperature sensitivity of the composite materials, static ultimate bending strength tests were conducted at each specific target temperature independently before fatigue testing. The applied cyclic stress amplitude was then calculated based on the respective ultimate strength at that specific temperature. The stress level was set to a constant value of 0.5, calculated as the ratio of the applied peak dynamic stress to the ultimate static strength at the corresponding temperature. The selection of a single stress level of 0.5 was made on the basis that it represents an intermediate stress state which accelerates fatigue damage accumulation without inducing immediate pseudo-static failure. This level of stress effectively represents the stress conditions of pavement structures under standard axle loads.

Furthermore, a single excitation frequency of 10 Hz is used to simulate the dynamic impacts of moving traffic; the corresponding equation is defined as (1):

$$t = \frac{L}{v} \tag{1}$$

where t is the loading duration, v is the simplified relationship between vehicle speed, and L is the tyre contact length. In standard pavement engineering practice, a 10 Hz frequency corresponds to a 0.1-s pulse duration, effectively simulating vehicles travelling at approximately 60–80 km/h under typical tyre contact conditions. The stress level was consistently adjusted to 0.5, with a stress ratio (R) of $\sigma_{\min}/\sigma_{\max} = 0.1$, keeping the minimum stress positive. The test was automatically terminated when the specimen fractured completely or when the system detected a load amplitude reduction greater than 30% of the peak load. Each temperature condition was examined using five parallel specimens.

2.4 Digital Image Correlation for Full-Field Strain Monitoring

A three-dimensional DIC system was employed, consisting of two 5-megapixel CMOS cameras with resolution 2448 × 2048, matched telecentric lenses, a high-brightness LED cold light source, and synchronous triggers. The cameras were mounted on a tripod at an approximate 25° angle, directly facing the transparent observation window of the temperature-controlled chamber. The image acquisition rate was set at 10 Hz (one DIC image frame was taken every 1000 loading cycles). Before testing, apply a very thin, even coat of matt white paint to the observation side of the test specimen to serve as a background layer, thereby preventing glare. Once the primer has dried, use a roller to apply black matt paint evenly. The camera was calibrated to ensure that the reprojection error was less than 0.03 pixels. For subsequent image post-processing and strain computation, a subset size of 121 × 121 to 125 × 125 pixels and a step size of 30 to 31 pixels were selected, depending on the speckle density of each specimen. Considering the heterogeneous nature of the composite interface and the requirement to capture highly localised strain gradients near the reflective crack tip, this parameter combination ensured a sufficient number of distinct speckles within each subset for reliable correlation while maintaining an optimal spatial resolution. A point-by-point local least-squares fitting algorithm was applied to the calculated displacement field to derive the strain components. In light of the constrained deformation and pronounced viscoplastic creep of the epoxy-bitumen binder at elevated temperatures, the Green-Lagrange strain tensor formula was utilised to meticulously ascertain the considerable geometric non-linearity of the strain within the interfacial transition zone.

2.5 Evaluation of Interfacial Fracture Toughness via J-Integral Approach

To characterise the fracture resistance of the rigid-flexible composite interface under varying thermal conditions, the interfacial fracture energy release rate (G_c) was determined using the J-integral approach based on elastic-plastic fracture mechanics (EPFM). This approach is predicated on the assumption that the energy dissipated during crack propagation incorporates both the surface energy required for crack extension and the viscoplastic dissipation at the crack tip.

The fracture energy (U) was obtained by integrating the area under the load-deflection (P-δ) hysteresis loop up to the point of macroscopic failure, representing the total work done by the applied load. Assuming the bulk energy dissipation is negligible compared to the localised energy dissipation at the composite interface, G_c was subsequently calculated using Eq. (2):

$$G_c = \frac{U}{A_{lig}} = \frac{\int_0^{\delta_f} P\, d\delta}{b\,(W - a)} \tag{2}$$

where P is the applied cyclic load, δ is the corresponding crosshead displacement, and δ_f is the displacement at failure. The parameter A_{lig} represents the effective uncracked ligament area of the interface, calculated from the specimen width (b), the specimen depth (W), and the initial notch or debonded length (a).

3 Results and Discussion

3.1 Effect of Temperature on Fatigue Life and Macro-Mechanical Response

The fatigue performance of the composite specimen structure, which consists of a cement concrete base layer and an epoxy-emulsified bitumen micro-surfacing, shows a strong temperature-dependent nonlinearity. As shown in Fig. 1 and Table 5, the fatigue life (N_f) followed a bell-shaped distribution curve over the investigated temperature range (−10°C to 45°C). At 15°C, the material reached excellent fatigue performance, with a fatigue life of around 9.0×10^4 cycles. When the temperature dropped to −10°C, fatigue life declined to 2.2×10^4 cycles, with N_f falling by approximately 78% from its peak. When the temperature reached 45°C, the fatigue life reduced to 8 × 10^3 cycles, with a peak life decrease of almost 90%. This occurrence suggests that two elements influence the composite specimens' interfacial failure mechanism: (1) embrittlement at low temperatures, and (2) softening at high temperatures.

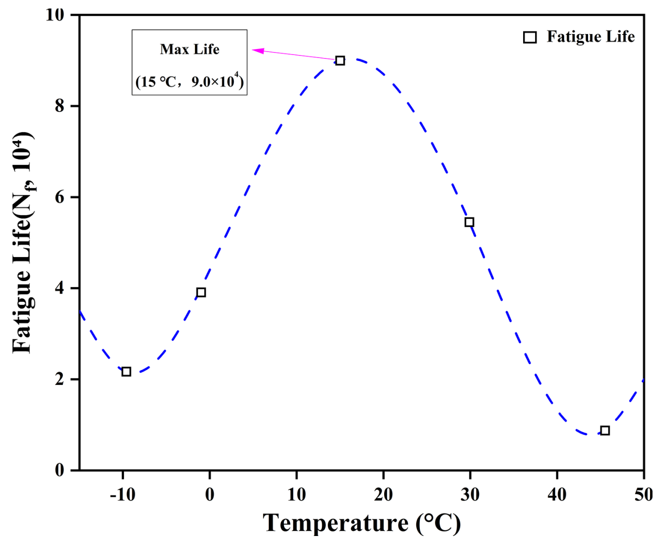

Figure 1: Fitting curve of fatigue life vs. temperature.

Table 5: Fatigue life of composite specimens at different temperatures.

Temperature (°C)	Cycle Count(N_f, 10^4)	Fatigue Type
−10	2.2	Low-temperature brittle fatigue
0	4.4	Brittle-ductile transition fatigue
15	9.0	Optimal viscoelastic fatigue
30	5.4	Viscoelastic softening fatigue
45	0.83	High-temperature shear fatigue

To further understand the underlying mechanical reaction that governs fatigue life evolution, Fig. 2a–e examines the progression of load-deflection hysteresis loops at various temperatures, while Fig. 2f gives a quantitative assessment of peak load and deflection. To ensure the reliability of these findings, all tests must be conducted on at least three replicate specimens per condition. The results obtained from these tests are to be presented as the mean ± standard deviation (SD). To verify the effect of temperature on fatigue performance, a one-way analysis of variance (ANOVA) was performed, followed by a Tukey's post hoc test.

The material exhibited exceptional stiffness at low temperatures of −10°C and 0°C, as evidenced by the steep starting slope in Fig. 2a,b. Load-deflection curves at −10°C showed strong sawtooth variations at peak loads, associated with fast and unstable crack propagation, localised brittle fracture, and spalling. This stochastic brittle behaviour resulted in a relatively high coefficient of variation (CV, approximately 15%) in fatigue life. This results from a lack of relaxation ability in the asphalt phase at low temperatures, which prevents effective stress dissipation. As a result, despite its great load-bearing capacity, the material is subject to rapid crack propagation and premature failure.

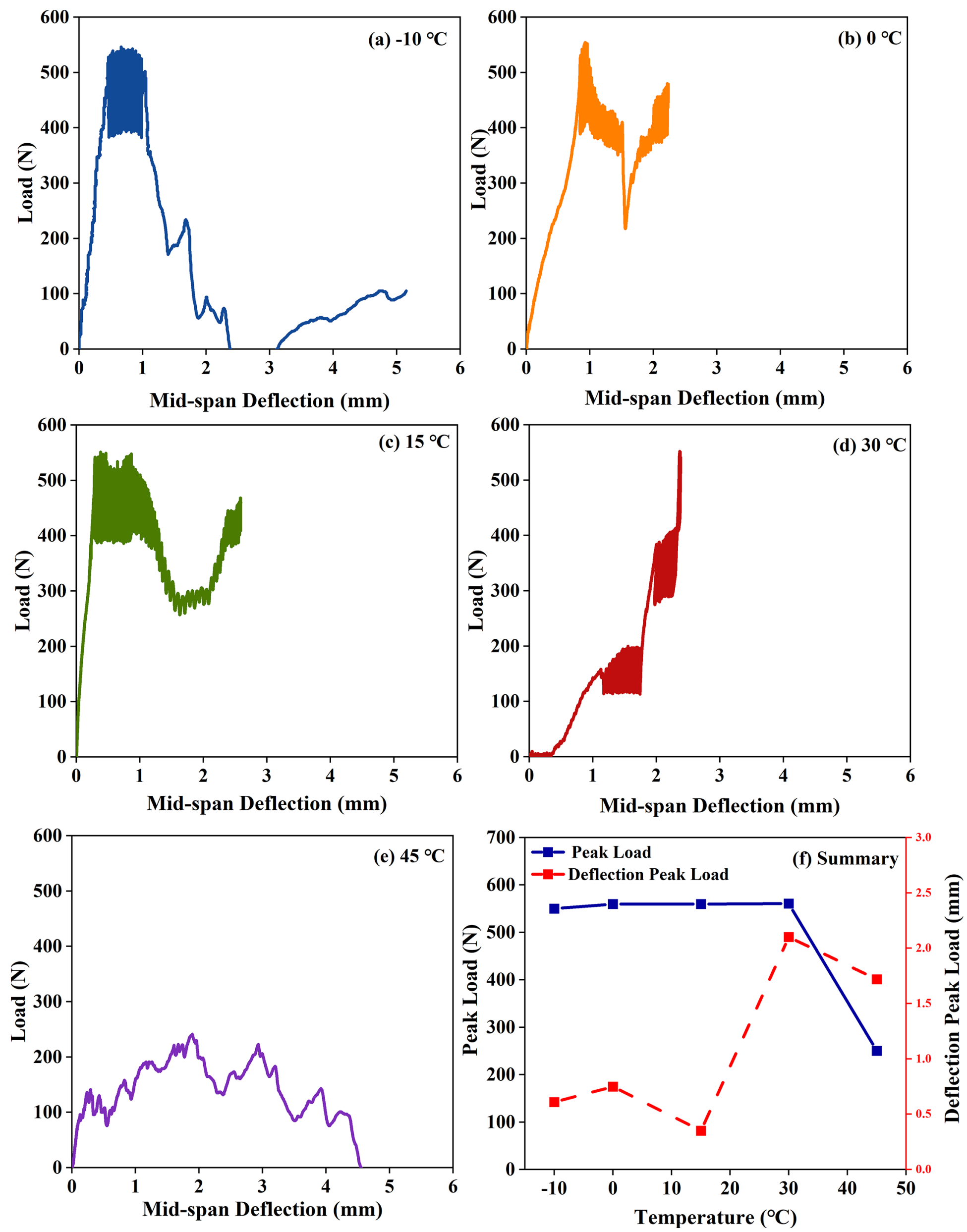

Figure 2: Load-deflection relationship curves at different temperatures: (**a**) −10°C; (**b**) 0°C; (**c**) 15°C; (**d**) 30°C; (**e**) 45°C; (**f**) summary diagram.

At 15°C, the material had the most stable mechanical response, with hysteresis loops inclining toward stability and low deflection at peak loading (about 0.4 ± 0.05 mm), indicating good deformation resistance, as shown in Fig. 2c,f. The findings suggested a synergistic interaction between the epoxy resin network and the asphalt phase. The epoxy resin network gave the material structural stiffness, while the asphalt phase retained enough flexibility to accommodate microstrains without causing brittle cracks. This results in an ideal mix of stiffness and ductility, thereby delaying the beginning of fatigue damage. This observation is consistent with the peak fatigue life shown in Fig. 1, which was statistically proven to be the maximum of the "bell-shaped" curve ($p < 0.05$ compared to extreme temperatures), exhibiting the lowest data dispersion CV < 8%).

At 30°C, although the epoxy resin network helped maintain load-bearing capacity with a peak load of approximately 560 ± 32 N, the material still exhibited excessive deformation, with peak deflection exceeding 2.0 ± 0.18 mm. Fig. 2d showed that viscoplastic flow and slip between aggregates begin as the bituminous binder softens. While the material keeps its strength, severe deformation accelerates the accumulation of fatigue damage, reducing its useful life.

As the temperature continued to climb to 45°C, the composite material exhibited severe high-temperature softening, with the peak load abruptly reducing to around 250 ± 28 N. This represented a statistically significant decrease of nearly 55% compared to 15°C ($p < 0.01$), as shown in Fig. 2e. This happened because the asphalt phase had lost significant cohesive strength, the interlocking force between aggregates was reduced, and the binder could no longer properly transmit stress, resulting in the worst fatigue performance and higher uncertainty in deformation measurements due to rheological instability.

3.2 Evolution of the Interfacial Shear Strain Field in DIC at Different Temperatures

To investigate the interface synergistic deformation mechanism of composite specimens, Digital Image Correlation (DIC) technology was employed to analyse the strain field at the interface between the cement concrete base layer and the epoxy-emulsified asphalt micro-surfacing at various temperatures. Fatigue loading was applied at three characteristic temperatures: −10°C, 15°C, and 45°C. Digital Image Correlation (DIC) was used to track the evolution of the horizontal strain field (ε_{xx}) at the composite specimen interface.

As shown in Fig. 3, under environmental conditions of −10°C, the strain evolution at the specimen interface exhibited distinct localisation characteristics. During the initial fatigue loading stage (Fig. 3a), the strain level in the interface region was extremely low and relatively uniformly distributed. As the number of load cycles increased (Fig. 3b), strain began to significantly concentrate in the interface region, gradually forming a strain band, with the maximum in-plane strain increasing to approximately 0.68%. As fatigue damage continued to accumulate, a localised region of high strain concentration eventually formed at the interface (Fig. 3c), with the peak in-plane strain surging to 2.64%. The peak horizontal strain (2.64%) shifts slightly from the geometric interface toward the asphalt binder phase. This is primarily due to severe modulus mismatch between rigid concrete and brittle asphalt. At −10°C, the asphalt phase transitions to a glassy state, characterised by a significant increase in elastic modulus and reduced stress relaxation capacity. This limits deformation coordination at the interface. The resulting stiffness disparity constrains deformation coordination at the boundary, forcing the interface to endure highly concentrated shear stresses. Since the material cannot dissipate accumulated energy through viscoelastic flow, interface stresses prematurely exceed bond strength, leading to unstable crack propagation and triggering macroscopic bond failure.

At 15°C, the evolution of the strain field reflected the viscoelastic transition characteristics of the material. During damage accumulation, the maximum strain gradually increased to approximately 1.5%. In comparison to low-temperature conditions, the diameter of the high-strain zone increases, and the strain gradient becomes more moderate, as shown in Fig. 4. At ambient temperatures, micro-surfacing materials had some stress relaxation capability, which helped to reduce stress concentration at interfaces. This suggested that the asphalt material near the interface experienced some degree of viscoelastic creep, reducing stress concentration. The failure mode had characteristics of both fracture propagation and local plastic deformation.

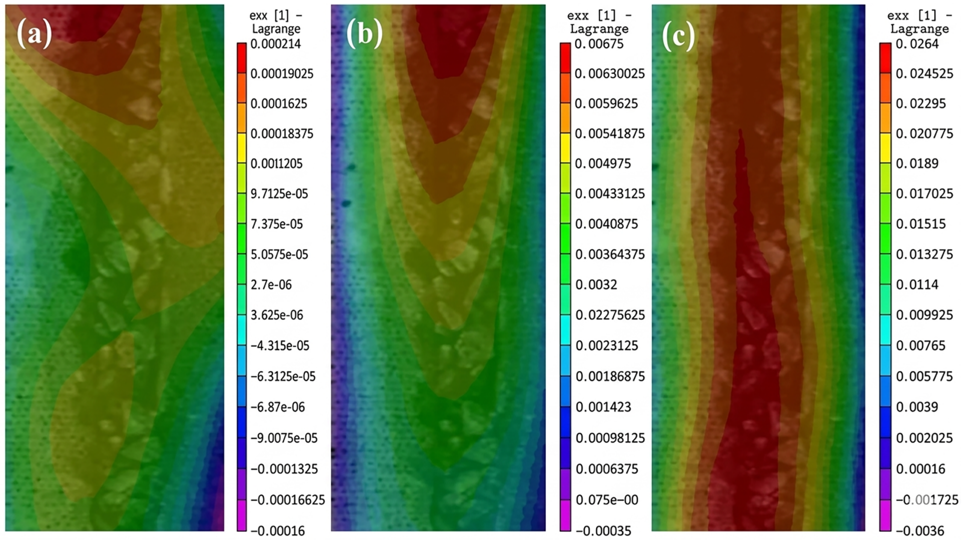

Figure 3: Evolution of horizontal strain (ε_{xx}) in the interface region at −10°C during fatigue loading: (**a**) 10% N_f; (**b**) 50% N_f; (**c**) 90% N_f.

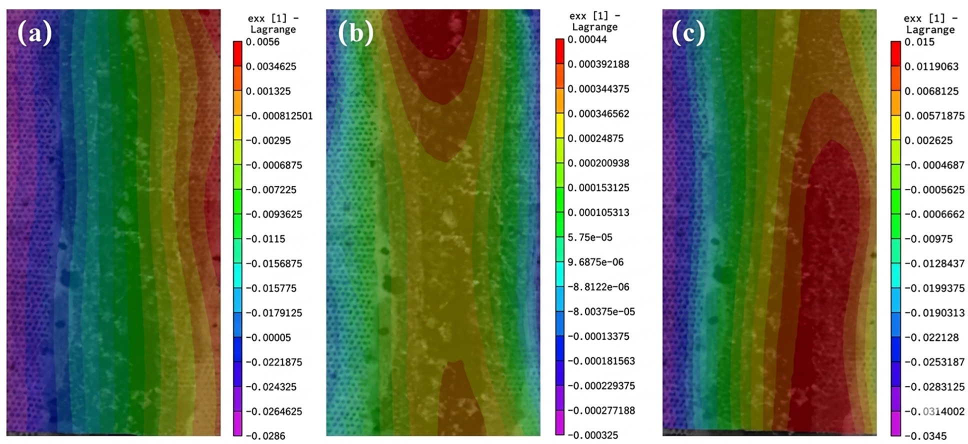

Figure 4: Evolution of horizontal strain (ε_{xx}) in the interface region at 15°C during fatigue loading: (**a**) 10% N_f; (**b**) 50% N_f; (**c**) 90% N_f.

At 45°C, the interfacial mechanical response changed qualitatively, with noticeable viscoplastic rheological properties. Strain contour graphs demonstrate no discrete crack zones, but rather large diffuse high-strain regions. During the initial loading phase (Fig. 5a), the maximum strain was 0.11, which eventually accumulated to 0.292, significantly surpassing the low-temperature fracture threshold shown in Fig. 5. This significant deformation indicates that interfacial failure is not caused by isolated fracture propagation, but rather by broad shear flow and permanent deformation throughout the matrix.

To quantify the degree of strain concentration during damage progression, Fig. 6 illustrates the evolution of the Stress Concentration Factor (SCF) at the interface between the cementitious concrete base course and the epoxy-emulsified asphalt micro-surfacing, plotted against the normalised fatigue life (N/N_f) at three temperature conditions: −10°C, 15°C and 45°C. The graphic showed that temperature had a considerable effect on the strain concentration behaviour at the contact. During the initial stage (about N/N_f < 0.4), the SCF stabilised around 1.0 at all three temperatures, indicating an intact interface with minimal damage accumulation and strain localisation.

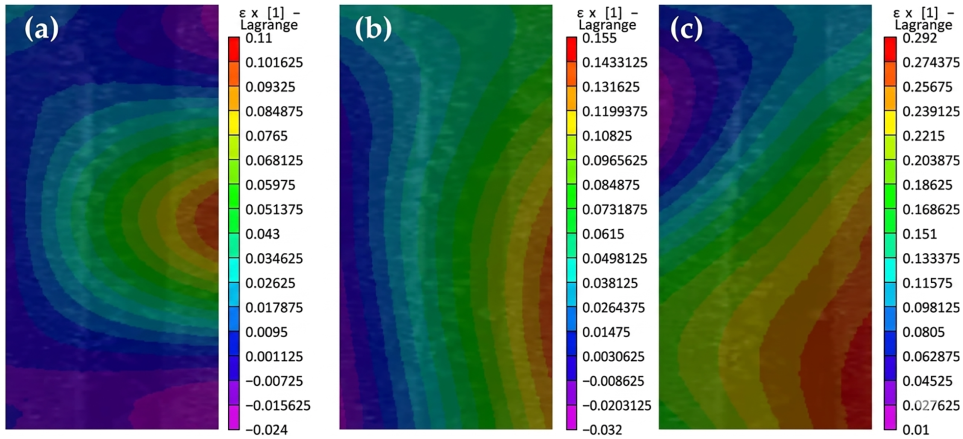

Figure 5: Evolution of horizontal strain (ε_{xx}) in the interface region at 45°C during fatigue loading: (**a**) 10% N_f; (**b**) 50% N_f; (**c**) 90% N_f.

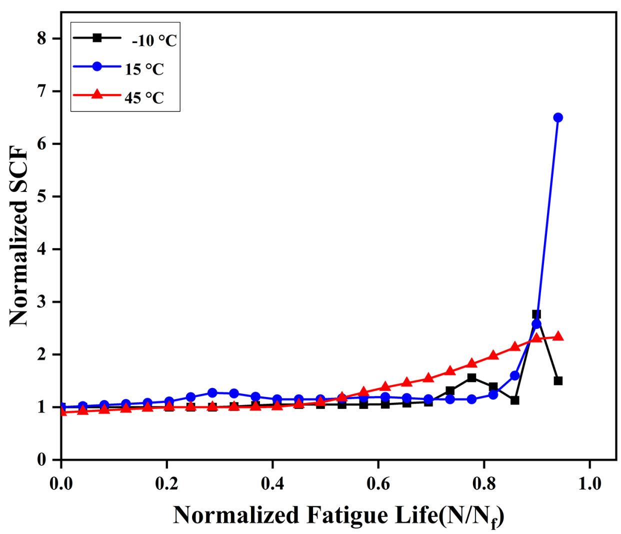

Figure 6: Evolution curve of the surface stress concentration factor (SCF) vs. normalised fatigue life.

As fatigue loading advanced, the interfacial behaviour changed dramatically due to the epoxy-emulsified bitumen's temperature-dependent viscoelastic characteristics. At −10°C, the SCF remained steady until the N/N_f ratio reached 0.7, at which point it entered an unstable expansion phase characterised by substantial variations and the emergence of localised peaks and troughs, eventually reaching around 3.0. This oscillating behaviour reflected the fragile nature of the contact at low temperatures. Strain energy can be released during the creation, stoppage, and re-initiation of microcracks, leading to the observed jagged evolution curve. The SCF was steady around 15°C during the early life stage. However, in the latter life stage ($N/N_f > 0.8$), the SCF demonstrated exponential expansion, with peak levels reaching 6. Extremely high SCF implies severe localised stress/strain concentration at the interface, resulting in microcracks or damage zones. Nonetheless, the specimen does not fracture quickly, indicating excellent damage tolerance at the contact at 15°C. The material blunts the fracture tip by localised micro-plastic deformation, allowing for significant local strains while maintaining structural load-bearing capacity. At temperatures over 45°C, SCF began to depart from the stable phase at $N/N_f = 0.5$, exhibiting a consistent and prolonged increase trend, eventually reaching roughly 2.2 before failing. This steady increase demonstrated that failure at high temperatures was caused by material softening and rheological failure across the specimen, rather than stress concentration. Damage buildup was mostly caused by viscoplastic deformation, which allowed for some stress dispersion, preventing abrupt strain spikes but resulting in a persistent increase in strain concentration. The slow and modest rise of SCF over the service life implies that viscous dissipation mechanisms are dominant, with broad plastic flow successfully mitigating stress concentrations. As a result, the interfacial strain concentration is highly temperature sensitive.

3.3 Fracture Toughness at the Interface

The interfacial fracture energy release rate (G_c) was determined via the J-integral approach to assess the fracture resistance of the interface under varying thermal conditions. Fig. 7 showed the variation in G_c at test temperatures of −10°C, 15°C, and 45°C. The results showed that interfacial bonding behaviour varied with temperature. At −10°C, the contact was brittle with a G_c value of 200.4 J/m^2. At 15°C, G_c gradually climbed to 405.5 J/m^2. At 45°C, fracture toughness increased to 1426.4 J/m^2, more than seven times higher than at −10°C. Regression analysis shows that Gc grows exponentially with temperature (T), as represented in Eq. (3):

$$G_c = 238.6 \times e^{0.040T} \left(R^2 > 0.99\right) \tag{3}$$

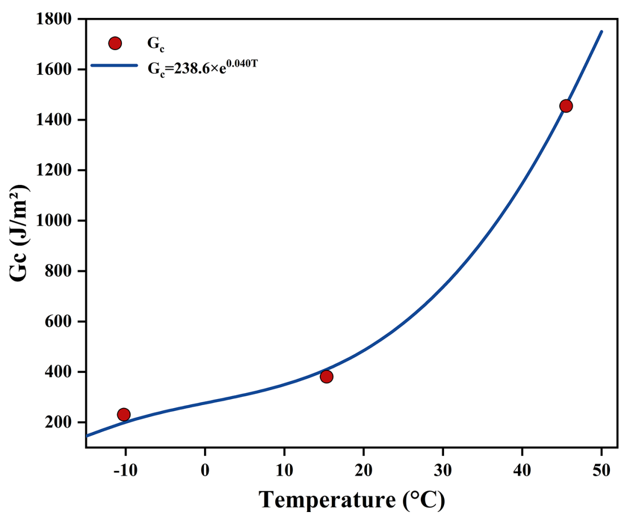

Figure 7: Temperature dependence of the boundary critical strain energy release rate (G_c).

The increase in the G_c toughness index observable in Fig. 7 and Table 6 can be attributed to the viscoelastic properties of the epoxy asphalt binder. At low temperatures, polymer chains remained in a confined frozen or glassy state, creating a tiny working zone at the crack tip where energy is predominantly released via direct bond breakdown. However, as the temperature climbed to 45°C, the binder gradually transitioned to a rubbery or viscous state. Thermal effects enhance molecular chain mobility, allowing for significant plastic deformation and viscous flow within the crack tip working zone. This significant plastic dissipation serves as a toughening mechanism, effectively blunting the crack tip and absorbing significant energy during crack propagation. As a result, G_c values increased exponentially at high temperatures.

However, under cyclic loading, this causes a rapid accumulation of viscoplastic strain (ratchet effect) and creep damage. Thus, exceptional fatigue endurance at 15°C results from an ideal balance of stiffness and ductility, but high-temperature failure is predominantly determined by creep-fatigue interaction rather than fracture toughness capacity.

Table 6: Mechanical performance, fatigue life, and fracture energy of the asphalt-concrete interface across various temperatures.

Temperature(°C)	Peak Load (N)	Maximum Deflection (mm)	Fatigue Life, N_f ($\times 10^4$)	Fracture Energy, G_c (J/m^2)
−10	~550	~0.5	2.2	200.4
0	~560	~0.6	4.4	–
15	~560	~0.4	9.0	405.5
30	~560	~2.2	5.4	–
45	~250	~1.7	0.83	1426.4

3.4 Macro Analysis of Interface Failure Modes

The macroscopic morphology of the ultimate shear failure surfaces at −10°C, 15°C, and 45°C was examined to investigate the effect of temperature on the failure interface of composite specimens consisting of cement concrete base layers and epoxy-emulsified asphalt micro-surfacing, as shown in Fig. 8. The failure mode at the interface might be established immediately by conducting a quantitative and qualitative study of residual binder distribution features and substrate exposure states within the fracture surfaces. This highlighted how temperature affects interlayer bonding performance.

At −10°C, the fracture surface showed substantial exposure of the greyish-white concrete substrate and reasonably smooth fracture features, as illustrated in Fig. 8a. At this temperature, the image revealed that asphalt coverage across the failure surface has decreased significantly. This indicated that, at low temperatures, the interface bond strength was insufficient to withstand shear forces. Cracks tend to spread along the concrete-asphalt junction, resulting in delamination of the asphalt layer from the base surface. The major failure mode was adhesive failure, indicating that the physicochemical bonding at the interlayer interface was the weak link in the composite structure. Fig. 8b displayed the failure interface characteristics at 15°C. The failure surface had a homogeneous and solid black look, with almost no exposed concrete substrate visible. At ambient temperatures, the epoxy resin's cured network structure had outstanding interfacial toughness with the asphalt. This produced an interfacial binding strength that was much greater than the shear strength of the micro-surfacing material. Cracks are pushed to propagate via the material's interior, resulting in optimal interfacial performance. As shown in Fig. 8c, even at 45°C, the failure surface retains a high level of asphalt cover, with cohesive failure remaining the dominant failure mode. However, the fracture surface texture becomes coarse, indicating rheological deformation. This occurred because elevated temperatures caused the asphalt binder to soften and its viscosity to decrease, resulting in pronounced viscoelastic-plastic behaviour. However, the micro-surfacing material itself exhibits reduced shear strength due to thermal softening, leading to shear yielding failure within the material matrix. Consequently, temperature emerges as the critical factor determining the failure mode as a significant element in determining the failure mode at the interface of cement concrete and epoxy-emulsified asphalt microsurfacing. At 15°C, the composite specimens demonstrate optimal interface performance.

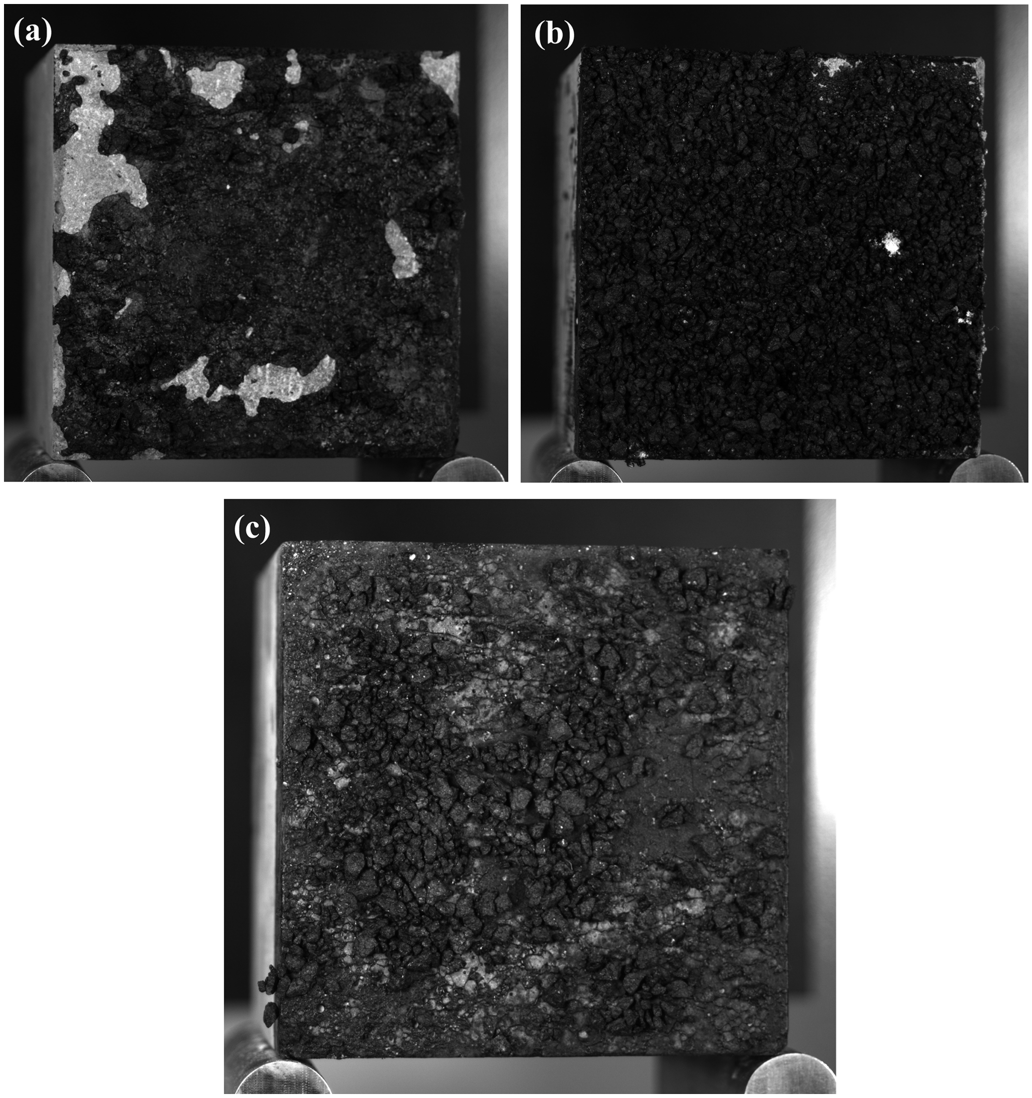

Figure 8: Macrographs of interfacial failure in composite specimens at different temperatures: (**a**) −10°C; (**b**) 15°C; (**c**) 45°C.

4 Conclusions

In conclusion, composite specimens were made with cement, river sand, crushed stone, high-performance epoxy emulsified bitumen, and aggregate grading (ISSA Type III) to create a cement concrete base course with an epoxy emulsified bitumen micro-surfacing overlay. Fatigue testing, digital image correlation (DIC) analysis, and fracture mechanics analysis were all performed on the composite specimens at different temperatures. Under the specific laboratory conditions tested, the fatigue life of composite specimens followed a bell-shaped distribution, with an optimal value of 9.0×10^4 cycles at 15°C. At −10°C, fatigue life diminishes by approximately 78% from its peak due to brittle fracture. At a high temperature of 45°C, severe viscoplastic deformation and shear flow due to matrix softening lead to a life loss of 90%.

At low temperatures, interfacial strain is extremely localised, resulting in limited zones of high strain gradient. The variable increase in the Stress Concentration Factor (SCF) reflected the unpredictable process of crack initiation, arrest, and re-propagation, which manifested macroscopically as adhesive failure at the interface. At room temperature, the material's stress-relaxation capability increases, extending the high-strain zone and flattening the gradient. This efficiently reduced stress concentration at the fracture tip, allowing cohesive failure at the interface under severe damage tolerance. At high temperatures, interfacial degradation evolved into a gradual accumulation process dominated by substantial shear flow. Although the interfacial fracture energy release rate (G_c) increased exponentially with temperature, culminating at 45°C, this was mostly due to considerable viscous dissipation and plastic deformation energy absorption at high temperatures, rather than true fatigue load-bearing capacity. The underlying failure process was the decrease of internal shear strength in the material.

In summary, the laboratory findings suggest that temperature governs phase transitions within the epoxy-emulsified asphalt micro-surfacing material (from a glassy state to a viscoelastic state and, eventually, a viscous flow state), dictating the composite structure's interfacial mechanical response and failure modes. The higher fatigue durability seen at 15°C is due to a key balance between material stiffness and ductility, which effectively suppresses both low-temperature brittle cracking and high-temperature plastic flow. However, it must be noted that these conclusions are drawn from a limited experimental scope. To fully translate these localised optimal temperature behaviours and failure mechanisms into practical engineering guidelines, further research involving complex multi-axial stress states, long-term environmental ageing, and comprehensive full-scale field validations is necessary.

Acknowledgement: Not applicable.

Funding Statement: This research was funded by the National Natural Science Foundation of China (NSFC) under Grant No. 52278226.

Author Contributions: The authors confirm contribution to the paper as follows: study conception and design: Dongjie Tan, Xinxin Cao; data collection: Dongjie Tan, Xiaoyu Yang; analysis and interpretation of results: Dongjie Tan, Xiaoyu Yang, Xinxin Cao; draft manuscript preparation: Dongjie Tan and Xinxin Cao. All authors reviewed and approved the final version of the manuscript.

Availability of Data and Materials: Data available on request from the authors. The data that support the findings of this study are available from the corresponding author, Xinxin Cao, upon reasonable request.

Ethics Approval: Not applicable.

Conflicts of Interest: The authors declare no conflicts of interest.

References

1. Wang F, Xiao Y, Cui P, Lin J, Li M, Chen Z. Correlation of asphalt performance indicators and aging Degrees: a review. Constr Build Mater. 2020;250(17):118824. doi:10.1016/j.conbuildmat.2020.118824.
2. Gransberg DD. Microsurfacing. In: National cooperative highway research program (NCHRP) synthesis 411. A synthesis of highway practice. Washington, DC, USA: National Academy of Sciences; 2010.
3. He L, Li S, Li W, Gu Y, Yang K, Dong L, et al. Performance evaluation of waterborne epoxy emulsified asphalt micro-surfacing with microwave-activated waste rubber powder. Constr Build Mater. 2024;413(1):134810. doi:10.1016/j.conbuildmat.2023.134810.
4. Leng Z, Ozer H, Al-Qadi IL, Carpenter SH. Interface bonding between hot-mix asphalt and various Portland cement concrete surfaces: laboratory assessment. Transp Res Rec J Transp Res Board. 2008;2057(1):46–53. doi:10.3141/2057-06.
5. Wei F, Cao J, Zhao H, Han B. Laboratory investigation on the interface bonding between Portland cement concrete pavement and asphalt overlay. Math Probl Eng. 2021;2021(1):8831287. doi:10.1155/2021/8831287.

6. Broughton B, Lee SJ, Kim YJ. 30 years of microsurfacing: a review. ISRN Civ Eng. 2012;2012(1171):279643. doi:10.5402/2012/279643.
7. Jiang X, Zeng C, Yao K, Gu HY, Li ZK, Qiu YJ. Influence of bonding conditions on flexible base asphalt pavement under non-uniform vertical loads. Int J Pavement Eng. 2021;22(12):1491–503. doi:10.1080/10298436.2019.1697441.
8. Raab C, Partl MN. Investigation into a long-term interlayer bonding of asphalt pavements. Balt J Road Bridge Eng. 2008;3(2):65–70. doi:10.3846/1822-427x.2008.3.65-70.
9. West R, Director P, Fan Gu P. Benefits of rehabilitating concrete pavements with slab fracturing and asphalt overlays, NCAT Report 20-03. Auburn, AL, USA: NACT; 2020 [cited 2026 Jan 1]. Available from: http://www.eng.auburn.edu/research/centers/ncat/files/technical-reports/rep20-03.pdf.
10. Baek J, Al-Qadi IL. Finite element modeling of reflective cracking under moving vehicular loading: investigation of the mechanism of reflective cracking in hot-mix asphalt overlays reinforced with interlayer systems. In: Airfield and highway pavements: efficient pavements supporting transportation's future. Bellevue, Washington, DC, USA: American Society of Civil Engineers; 2008. p. 74–85. doi:10.1061/41005(329)7.
11. Jiao L, Wu R, Harvey J. Reflective crack initiation of asphalt overlays on jointed concrete pavement using finite element model. Int J Pavement Eng. 2023;24(2):2154350. doi:10.1080/10298436.2022.2154350.
12. Zhou F, Scullion T. Overlay tester: a rapid performance-related crack resistance test. College Station, TX, USA: Texas Transportation Institute, Texas A & M University System; 2005 [cited 2026 Jan 1]. Available from: https://library.ctr.utexas.edu/hostedpdfs/tti/0-4467-2.pdf.
13. Kabir R, Hiller JE. Numerical analyses of rigid and flexible pavements responses under heavy vehicles' loading. Road Mater Pavement Des. 2021;22(2):333–56. doi:10.1080/14680629.2019.1621189.
14. Arsenie IM, Chazallon C, Duchez JL, Hornych P. Laboratory characterisation of the fatigue behaviour of a glass fibre grid-reinforced asphalt concrete using 4PB tests. Road Mater Pavement Des. 2017;18(1):168–80. doi:10.1080/14680629.2016.1163280.
15. Busang S, Maina J. Influence of aggregates properties on microstructural properties and mechanical performance of asphalt mixtures. Constr Build Mater. 2022;318(10):126002. doi:10.1016/j.conbuildmat.2021.126002.
16. Zeng Z, Sudarsanan N, Underwood BS, Kim YR, Guddati M. Reflective cracking performance evaluations of highly polymer-modified asphalt mixture. J Transp Eng Part B Pavements. 2024;150(3):04024039. doi:10.1061/jpeodx.pveng-1566.
17. Saride S, Kumar VV. Influence of geosynthetic-interlayers on the performance of asphalt overlays on pre-cracked pavements. Geotext Geomembr. 2017;45(3):184–96. doi:10.1016/j.geotexmem.2017.01.010.
18. Albayati AH, Mustafa FS, Al-ani AF, Sukhija M, Moudhafar MM, Maher AM. Advancing asphalt binder performance through nanomaterial and polymer modification: experimental and statistical insights. Results Eng. 2025;25(24):104458. doi:10.1016/j.rineng.2025.104458.
19. Zhou JY, Liu H, Zhang J, Wang X. Progress in fatigue performance evaluation and damage mechanisms of fibre-reinforced polymer composites. Chin J Theor Appl Mech. 2026;58(4):829–48. doi:10.6052/0459-1879-25-400.
20. Bhasin A, Little DN. Characterization of aggregate surface energy using the universal sorption device. J Mater Civ Eng. 2007;19(8):634–41. doi:10.1061/(asce)0899-1561(2007)19:.
21. Ghorbani R, Matta F, Sutton MA. Full-field deformation measurement and crack mapping on confined masonry walls using digital image correlation. Exp Mech. 2015;55(1):227–43. doi:10.1007/s11340-014-9906-y.
22. Sudarsanan N, Zeng ZA, Kim YR. Laboratory investigation into the crack propagation mechanism of geosynthetic reinforced asphalt concrete using digital image correlation technique. Int J Pavement Eng. 2023;24(1):2251079. doi:10.1080/10298436.2023.2251079.
23. Ren D, Yang H, Xu J, Wu P, Huang Y, Kong L, et al. Investigation on fatigue damage of Buton rock asphalt mixtures using semi-circular bending (SCB) and digital image correlation (DIC) techniques. Constr Build Mater. 2024;451:138797. doi:10.1016/j.conbuildmat.2024.138797.
24. Seo Y, Kim YR, Schapery RA, Witczak MW, Bonaquist R. A study of crack-tip deformation and crack growth in asphalt concrete using fracture mechanics. J Assoc Asph Paving Technol. 2004;73:697–730.
25. Huang Y, He X, Wang Q, Xiao J. Deformation field and crack analyses of concrete using digital image correlation method. Front Struct Civ Eng. 2019;13(5):1183–99. doi:10.1007/s11709-019-0545-3.